ACS Energy LETTERS

http://pubs.acs.org/journal/aelccp

Lattice Expansion Enables Large Surface Carrier Diffusion in WS_2 Monolayer

Lijie Wang, Yue Liu, Jie Yang, Xiangming Xu, Bingyao Shao, Hongwei Zhu, Haiting Cai, Tulai Sun, Jun Yin, Husam N. Alshareef, Osman M. Bakr, Yihan Zhu,* and Omar F. Mohammed*

Cite This: *ACS Energy Lett.* 2025, 10, 1741−1750

Read Online

ACCESS | Metrics & More | Article Recommendations | Supporting Information

ABSTRACT: Two-dimensional (2D) materials hold great promise for next-generation optoelectronic devices, with photogenerated charge carrier transport being critical to their performance. However, the influence of photoexcitation-induced commensurate lattice thermal effects on surface charge carrier dynamics is poorly understood. Traditional photon-pump/photon-probe methods have constraints in capturing the subtle yet critical surface dynamics, especially for these ultrathin materials due to challenges in spatial resolution and penetration depth. In this study, we utilized scanning ultrafast electron microscopy (SUEM), a technique that offers unparalleled sensitivity to surface phenomena that are entirely inaccessible through other methods. Our findings reveal a ∼1.4% negative thermal expansion at elevated temperatures, inducing internal strain that modifies the electronic structure and significantly enhances surface carrier transport, resulting in an order-of-magnitude improvement in photodetection performance. Moreover, we demonstrate that photoinduced charge carrier diffusion occurs predominantly within the first tens of picoseconds after photoexcitation, a regime characterized by thermal excitation resulting from carrier−phonon interactions. These results establish a direct link among lattice thermal expansion, carrier dynamics, and optoelectronic performance.

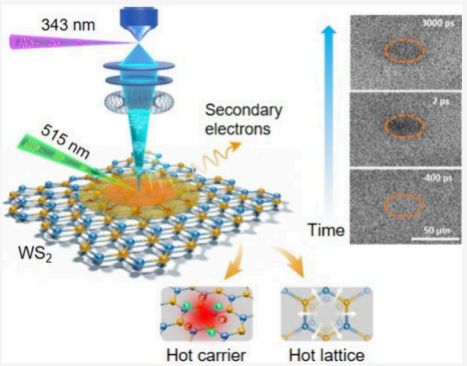

Atomically thin semiconductors, particularly two-dimensional (2D) transition metal dichalcogenides (TMDs), have emerged as a powerful platform for exploring nanoscale quantum phenomena and hold significant promise for optoelectronic applications,[1−5] including photodetectors, photovoltaics, transistors, and LEDs. These materials are characterized by remarkable excitonic properties, which arise from reduced dielectric screening, quantum confinement and enhanced Coulomb interactions due to their atomic-scale thickness.[6,7] A critical aspect in their practical application is the transport performance of photogenerated charge carriers.[8,9]

Traditionally, this has been investigated using indirect spectroscopic methods,[10−13] as exemplified by photoluminescence quenching and terahertz photoconductivity, which provide inferred values for carrier mobilities or diffusion constants of the bulk, often resulting in inconsistent results. Key factors[14−17] such as carrier lifetime, mobility, material band structure, and the presence of defects and impurities are widely recognized to influence the transport behavior of photogenerated charge carriers. For instance, transient reflection spectroscopy has demonstrated that grain boundaries and structural defects in monolayer MoS_2 act as scattering centers, thereby constraining carrier mobility.[18] Time-resolved photoluminescence (TRPL) further reveals substantial variability in exciton lifetimes and recombination rates, emphasizing the impact of nonradiative defect sites in reducing charge transport efficiency.[19] These observations highlight the heterogeneity of charge transport dynamics and underscore the need for spatially resolved techniques capable of probing localized transport phenomena at the nanoscale. Recent advancements in transient absorption microscopy (TAM) have facilitated the direct tracking of carrier transport in both spatial and temporal domains.[20−22] TAM has visualized ultrafast exciton diffusion in both monolayer and bulk $MoSe_2$, with diffusion coefficients of approximately 12 and 20 cm^2/s, respectively.[23] While TAM effectively maps carrier dynamics by detecting changes in absorption spectra, it typically requires models to interpret the experimental data and lacks the sensitivity needed to capture surface states, which are essential for influencing carrier transport in semiconductor materials.[24]

In this study, we utilize scanning ultrafast electron microscopy (SUEM) to achieve spatiotemporal imaging of

Received: January 27, 2025
Revised: February 28, 2025
Accepted: March 12, 2025
Published: March 17, 2025

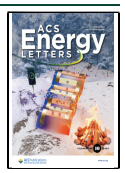

https://doi.org/10.1021/acsenergylett.5c00307
ACS Energy Lett. 2025, 10, 1741−1750

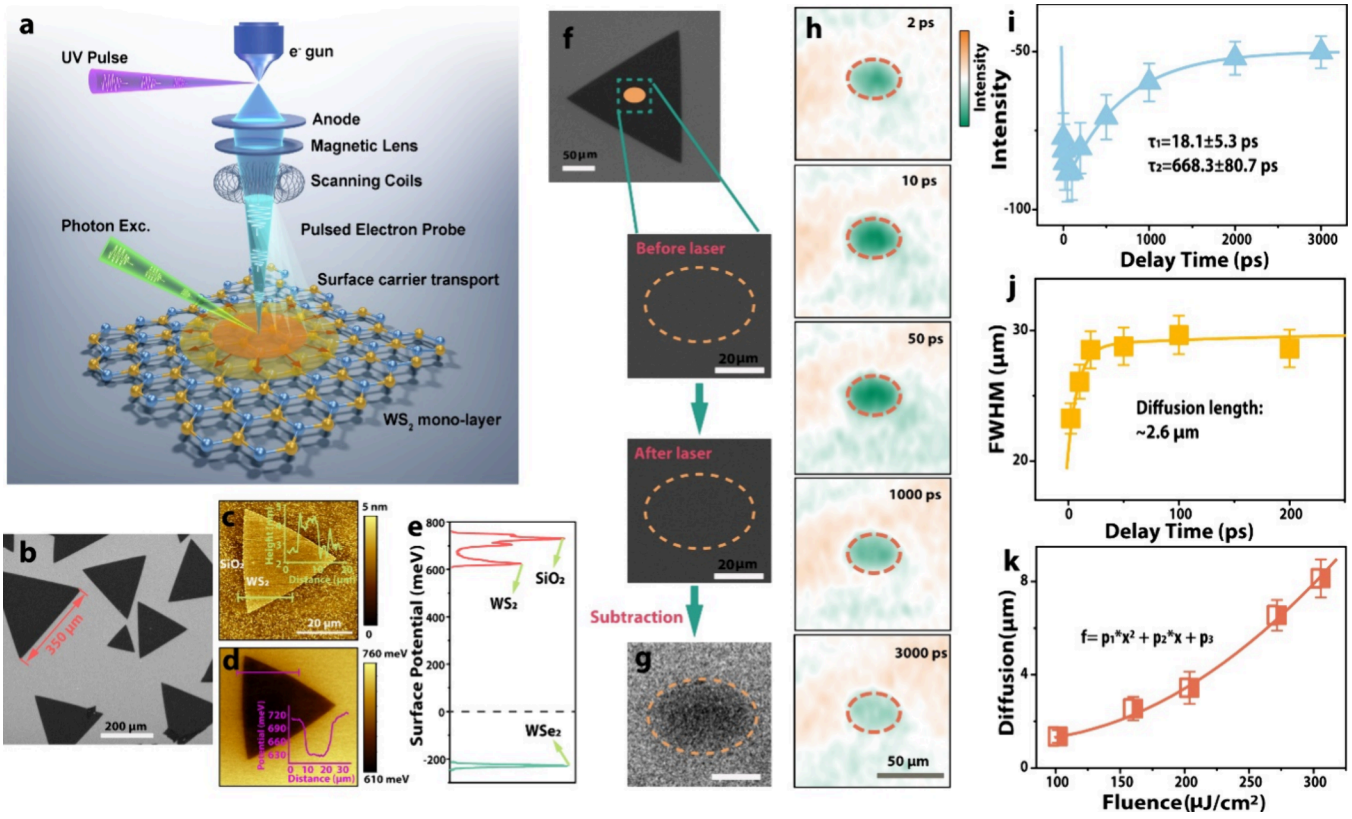

Figure 1. SUEM measurement of monolayer WS_2. a, Schematic illustration of probing photogenerated charge carriers via SUEM. Photon pulses are used to excite the sample, while electron pulses, generated by a delayed UV pulse (345 nm), probe the surface changes. b, SEM image of the monolayer WS_2 sample on a SiO_2/Si substrate, indicating crystal size ranging from ~50 to ~350 μm. c, AFM topography image of a monolayer WS_2 triangle with a step height of ~1 nm. d, Corresponding map of surface potential. The inset shows the potentials at the top of the triangle. e, Surface potential distribution values between WS_2, SiO_2, and a reference WSe_2 bulk crystal. f, SUEM images showing the region before and after excitation. The dashed ellipses represent the laser footprint. g, Example showing the SUEM difference signal, obtained by subtracting the SUEM images before and after excitation. h, Difference SUEM images illustrating the evolution of photoinduced carrier transport in the monolayer WS_2 sample. These images are derived from SUEM images at specific delay times, subtracting a reference image at a far negative time scale. Each image represents an average of 4 images at the same delay time. i, Evolution of the deduced SUEM signal intensity as a function of delay time. j, Evolution of the full width at half maximum (FWHM) as a function of delay time. k, Calculated diffusion distances under different excitation fluences. The diffusion is calculated using half of the difference in FWHM ($(FWHM_{100\ ps} - FWHM_{2\ ps})/2$).

carrier dynamics in monolayer WS_2, leveraging SUEM's unique surface sensitivity to investigate the underlying processes driving photoinduced carrier diffusion.[25−27] Our findings reveal that charge carrier diffusion predominantly occurs within the initial tens of picoseconds (ps) after photoexcitation, a period during which the material remains thermally excited as carrier energy dissipates as heat, increasing the lattice temperature. The increase in temperature induces lattice negative thermal expansion, as demonstrated by *in situ* scanning transmission electron microscopy (STEM). This internal strain alters the electronic structure and reduces the effective masses of charge carriers, significantly enhancing their transport efficiency. These new insights into the enhancement of charge carrier transport driven by lattice thermal expansion offer a deeper understanding of the complex mechanisms governing charge transport in 2D materials, illuminating the crucial role of lattice dynamics in shaping ultrafast surface-level charge transport and its implications for future optoelectronic applications.

Figure 1a presents a schematic illustration of the process used to probe photogenerated charge carriers in monolayer WS_2 via SUEM. The experimental setup integrates a modified scanning electron microscope (SEM) with a fs fiber laser system, with further details provided in the experimental section. One of the key modifications to SEM is the utilization of UV photon pulses to generate pulsed electrons, replacing the conventional continuous thermal electron source. Upon laser irradiation, hot charge carriers are generated and rapidly diffuse into the surrounding regions, exhibiting a Gaussian-like distribution in both space and time with the highest intensity at the center of the laser spot. The pulsed electron beams interacts with monolayer WS_2, generating secondary electrons (SEs), which are emitted from the uppermost layers of the surface in a manner highly sensitive to the local electron/hole density, enabling direct, high-resolution mapping of carrier diffusion dynamics.[28]

The morphological characteristics of the as-prepared WS_2 samples were investigated by using steady-state SEM and atomic force microscopy (AFM). Figure 1b displays the SEM image of monolayer WS_2 samples on a SiO_2/Si substrate, revealing well-dispersed crystals with equilateral triangle side lengths ranging from ~50 to ~350 μm. A small crystal was selected for a comprehensive surface morphology scan via AFM, as shown in Figure 1c. The scale bar, ranging from 0 to 5

https://doi.org/10.1021/acsenergylett.5c00307
ACS Energy Lett. 2025, 10, 1741−1750

nm on the right side, represents the surface roughness. The WS_2 crystal displays a distinct boundary and exhibits remarkable surface flatness. A cross-sectional profile taken at the corner of the triangle (indicated by the green line in Figure 1c) shows that the crystal height is approximately 1 nm despite a relatively high noise level in the measurement. Additionally, the surface potential of the same WS_2 crystal was measured using Kelvin probe force microscopy (KPFM) and compared to a reference WSe_2 bulk crystal, as the surface potential properties are crucial for determining the signal contrast in subsequent SUEM experiments. In Figure 1d, the WS_2 and SiO_2 substrates display distinct contact potential differences, with the WS_2 showing a low value and the SiO_2 showing a high value, differing by ∼90 meV. The surface potential distribution profiles for the WS_2, SiO_2 substrate, and reference WSe_2 are presented in Figure 1e. Compared to WSe_2, which exhibits a −220 meV value and a bright SUEM contrast (Figure S1), WS_2 shows a significantly higher positive value of ∼630 meV, indicating a different SUEM signal contrast behavior, which will be discussed later.

Figure 1 panels f and g illustrate the method used to generate the SUEM difference images. In Figure 1f, dashed ellipses on the WS_2 triangle surface before and after excitation indicate the laser excitation region. Importantly, no visible laser-induced damage was observed, even at the highest fluence used, indicating that the SUEM experiments remained below the sample's damage threshold. The SUEM difference images, obtained by subtracting the two (Figure 1g), reveal a distinct "dark" contrast in the WS_2, in contrast to the bulk WSe_2 (Figure S1). In this context, "dark/negative" refers to signal values that fall below the background baseline. This phenomenon, which has been reported in previous studies,[29−31] is attributed to multiple mechanisms and is likely due to the presence of different surface potentials on the studied samples. Figure 1h shows representative color-coded SUEM difference maps (see Figure S2 for the experimental time-resolved SUEM difference images), depicting the evolution of photoinduced charge carrier transport on the surface of a WS_2 crystal. The excited spots exhibit slightly elliptical shapes due to the pump laser being incident on the sample at a 54° angle. Each image represents an average of four images taken at the same delay time to enhance the signal intensity, with a consistent scale bar displayed on the right side for all images. In the color coding, orange indicates a high differential signal intensity, while dark green represents relatively low intensity. As the photon pulses arrive and the delay time increases, a distinct Gaussian-like "negative" signal begins to emerge and intensify. It is assumed that the image captured at ∼2 ps reflects the laser footprint, given the relatively long pulse duration and the gradual signal buildup process following excitation (the temporal resolution in this experiment is determined by the number of photogenerated electrons per pulse at the emitter source, in the present case, it was estimated to be 1.5 ± 0.3 ps; see Methods). We later used it as a reference to estimate the diffusion distances at different time delays.

The accurate transient response analysis is better highlighted by extracting a spatial profile from the center of the spot, thereby capturing the actual peak evolution in a Gaussian-like curve, as shown in Figure S3. This approach enables more detailed fitting to obtain parameters that describe the extent of peak broadening and the evolution of the signal intensity over time. The yellow solid lines represent the original experimental data, while the red-orange lines depict the fitted curves, which include a linear component for the background and a Gaussian function for the signal distribution, as expressed by

$$G(x) = a\frac{1}{\sigma\sqrt{2\pi}}e^{-x^2/2\sigma^2} + bx + c$$

The relative intensities at the peak position, plotted as a function of time delays, are presented in Figure 1i, alongside a biexponential fit. The evolution of the Full Width at Half Maximum (FWHM) of the fitted results is shown in Figure 1j, with an extended time window displayed in Figure S4. It is evident that the photoinduced signal intensity arises immediately after excitation and gradually diminishes over hundreds to thousands of picoseconds due to electron−hole recombination. The relative diffusion distance of ∼2.6 μm is determined from the change in FWHM, calculated based on $2\sigma\sqrt{2\ln(2)}$. The fitted time constants of the FWHM curve are 9.4 ± 1.1 and 200.0 ± 20.1 ps, respectively, indicating that photoinduced carrier diffusion predominantly occurs within tens of picoseconds, with negligible carrier transport thereafter. This time scale corresponds closely with the period for photoinduced electron−lattice coupling, which is typically a few to several tens of ps but varies depending on the excitation fluence (see Note S1). These findings prompt further investigation into the effects of the hot lattice and excitation power on charge carrier diffusion.

We next conducted excitation-fluence-dependent SUEM measurements on monolayer WS_2 samples. Figure S5 panels a and b present the SUEM difference images recorded at ∼2 and 100 ps under varying excitation powers, while Figure S5c displays the modeled Gaussian curves after background signal removal, representing carrier distribution at specific time delays. This approach allows for a direct comparison of the Gaussian-like signal width development at the corresponding excitation fluences. As expected, with increasing excitation power and enhanced thermal effects, the laser footprint becomes more intense and broader, as evidenced by the FWHM change at ∼2 ps, which increases from ∼17.7 μm at a fluence of ∼102 $\mu J/cm^2$ to ∼29.1 μm at ∼306 $\mu J/cm^2$. Although the pump power increased 3-fold, the initial laser-induced spot size enlarged by only about 1.6 times. However, the spot sizes at 100 ps, representing carrier diffusion relative to that at ∼2 ps, increased by approximately 2.5 times, from ∼20.5 to ∼45.3 μm. Diffusion was then estimated using half the difference in FWHM ($(FWHM_{100\ ps} - FWHM_{2\ ps})/2$), as demonstrated in the inset of Figure S5c. Figure 1k plots the calculated diffusion distances under different excitation fluences, which can be fitted with a nonlinear polynomial function (see the inset). This suggests that the enhancement of carrier transport is not directly proportional to the intensity of incident light, indicating that photoinduced effects, such as the temperatures of charge carriers and the lattice, could make an additional contribution in WS_2.

To confirm the photoinduced thermal effects, transient reflectivity (TR) measurements were performed across the visible spectral range. The experimental TR map under 400 nm excitation is presented in Figure S6a, with a focus on the first exciton peak at ∼630 nm and its surrounding spectral region. Figure S6b shows the reconstructed data based on lifetime density analysis (see Note S4 and Figure S6c for the fitting residuals). This analysis produces a lifetime distribution, offering a detailed and comprehensive view of the kinetics by

https://doi.org/10.1021/acsenergylett.5c00307
ACS Energy Lett. 2025, 10, 1741−1750

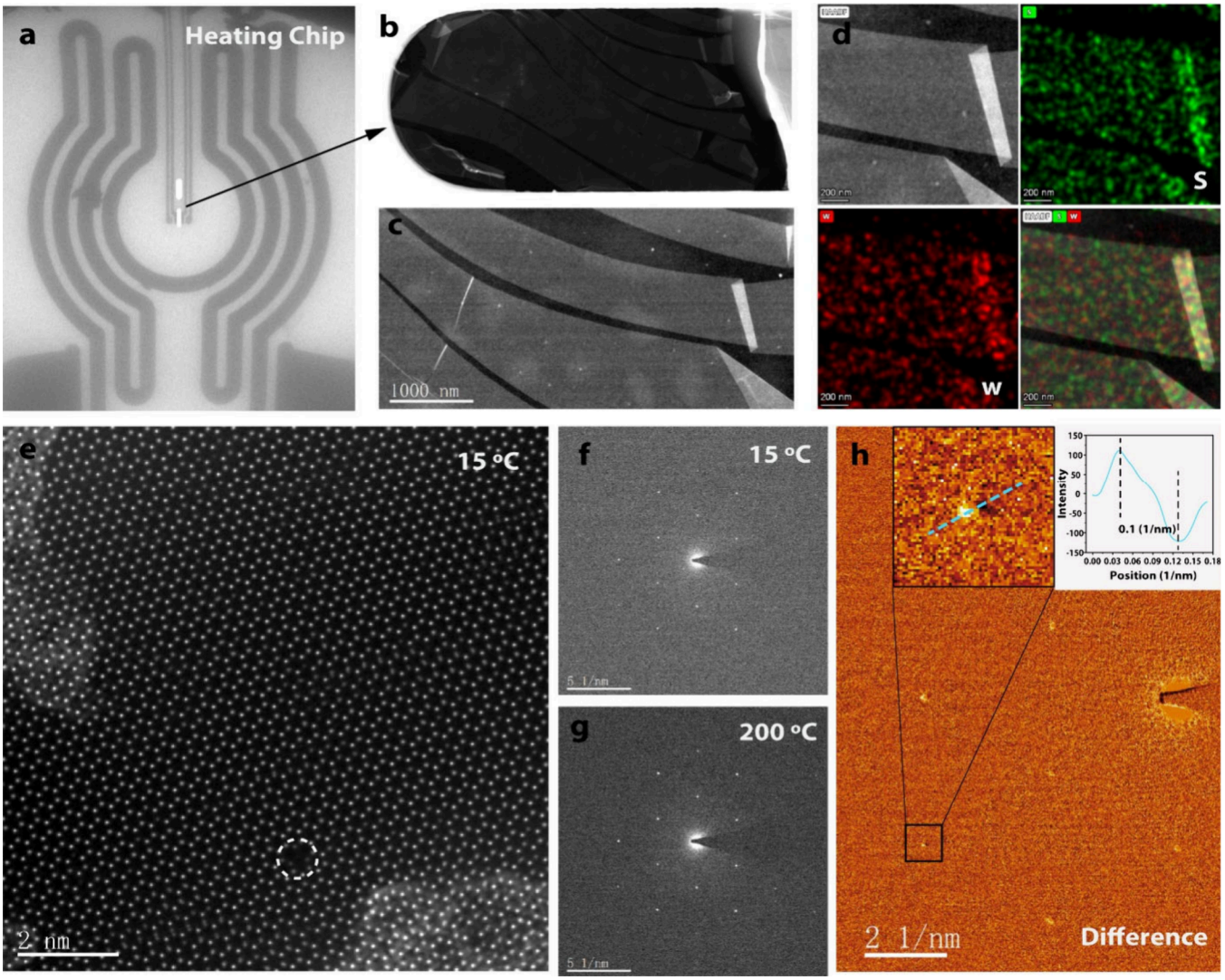

Figure 2. ***In-situ*** **heating TEM experiment on monolayer WS_2. a, TEM image of the heating chip unit. b, Enlarged region of the sample area in the heating chip. c, STEM image of the transferred monolayer WS_2 sample, with some cracks likely introduced during the transfer process. These cracks, commonly seen in *in situ* heating experiments, are on the μm scale and do not affect the imaging results, especially at very high magnification and atomic resolution imaging. d, Elemental mapping of the WS_2 sample, with sulfur (S) in green and tungsten (W) in red. e, Super-resolution electron ptychography image of the WS_2 monolayer sample at 15 °C temperature. The white dashed circle indicates the region where point defects are observed. f, Selected area electron diffraction (SAED) pattern of the sample recorded at 15 °C. g, SAED pattern of the sample recorded at 200 °C. h, Difference SAED image generated by subtracting the 15 °C pattern from the 200 °C pattern. The inset in the top left shows an enlarged region of the difference SAED pattern illustrating the change of the lattice spacing assigned to a high-order reflection, while the top right inset provides a linear intensity profile for the difference pattern of the reflection.**

resolving various spatial, energetic, and temporal degrees of freedom into a distribution map. A total of 20 lifetime constants were assumed, ranging from 0.03 to 5000 ps, with the resulting map displayed in Figure S6e. This map serves as a quasi-continuous analogue to the decay-associated spectra (DAS, Figure S6d) that obtained from global lifetime fitting, where the intense regions represent the most probable time constants at the respective detection wavelengths. Three distinct dynamical processes following photoexcitation, indicated by green dashed lines, can be identified: (1) carrier−carrier interactions with a time constant of ∼0.6 ps; (2) carrier−phonon coupling, leading to a lattice temperature increase with a time constant of ∼3.6 ps, accompanied by a red shift of the negative peak; and (3) lattice cooling with a time constant of ∼26.2 ps, as the negative peak shifts back to its initial position. This trend of lattice temperature increase followed by a decrease within a tens-of-ps window is consistent with observations in perovskite materials.[32]

The recorded transients at various pump fluences also reflect the temperature-induced profile changes. Figure S7a displays the spectral traces at 5 ps, with the inset showing a linear relationship between the peak intensity around ∼630 nm and the pump fluence. The TR spectra reveal two prominent negative bands at ∼630 and ∼520 nm, accompanied by a broad positive feature spanning from 525 to 620 nm. With increasing excitation fluence, both negative peaks, particularly the lower-energy one, shift toward the lower energy side. At the highest fluence of 500 μJ/cm^2, there is a pronounced increase in the intensity of the positive spectral feature on the higher-energy side, which could be related to strong changes in the refractive index due to local temperature increases.[33−35] Furthermore, we plotted the normalized kinetic traces at ∼630

https://doi.org/10.1021/acsenergylett.5c00307
ACS Energy Lett. 2025, 10, 1741−1750

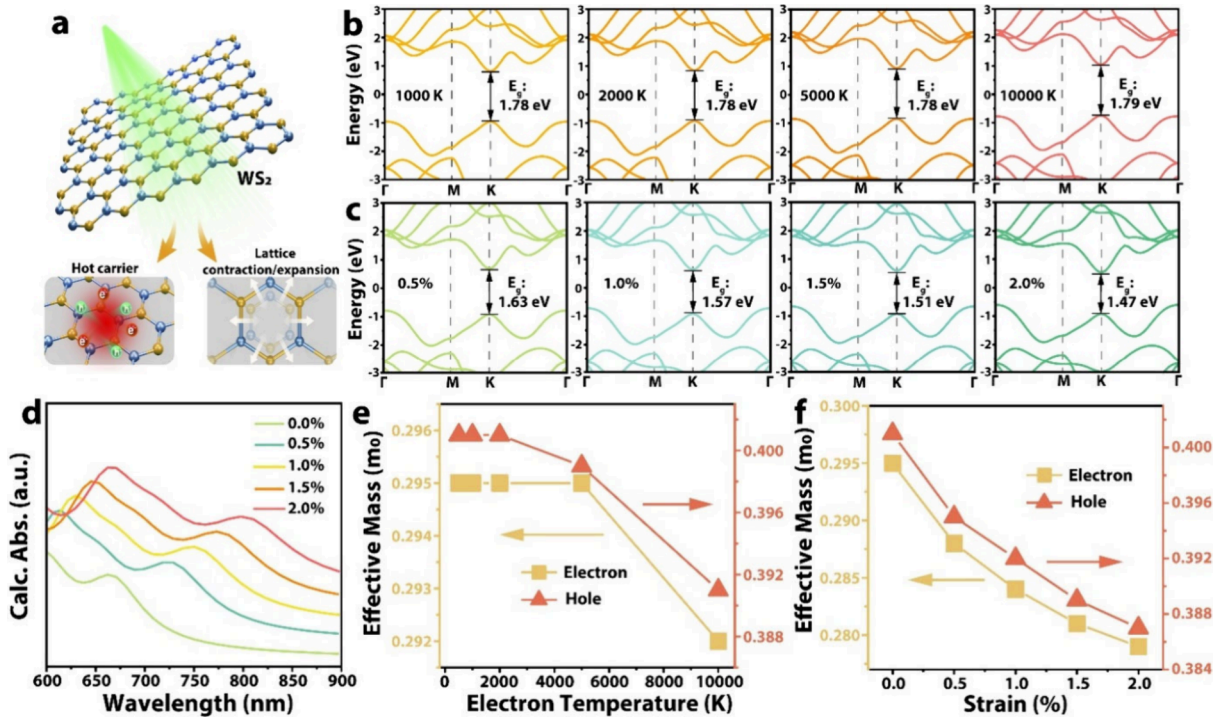

Figure 3. Calculated band structures, absorption, and effective masses of monolayer WS_2. a, Schematic illustrating WS_2 samples under light excitation, generating hot carriers and lattice thermal effects. b, Electronic band structures of monolayer WS_2 as a function of electron temperatures. c, Electronic band structures of monolayer WS_2 as a function of applied strains. The energy gaps at the K point are also labeled. d, Calculated absorption of monolayer WS_2 as a function of applied tensile strains. e, The calculated effective mass of electrons and holes in WS_2 at different electron temperatures. f, Calculated effective mass of electrons and holes at different level of strains.

nm under different excitation fluences, along with their corresponding fittings, as shown in Figure S7b. The fitted time constants, representing the decay of the signal and reflecting carrier recombination and thermal relaxation processes, are listed in Table S1. As the excitation fluence increases, the long-term time constants significantly rise, from 13.9 ± 3.3 and 197.1 ± 15.5 ps to 38.8 ± 7.3 and 390.5 ± 45.0 ps, respectively. This suggests that higher fluences, which are associated with increased lattice temperatures, may enhance electron−hole separation and extend the charge carrier lifetimes. This occurs despite the presence of other processes, such as Auger recombination, which is less prominent compared to its multilayer counterpart.[36]

The thermal effects on the crystal lattice of monolayer WS_2 are further investigated through *in situ* heating experiments using STEM. A monolayer WS_2 specimen has been transferred to a heating chip, as shown in Figure 2a, with the heating spiral encircling the sample area. Figure 2b provides a magnified view of the thin specimen, imaged with bright contrast by using the annular dark field (ADF) STEM mode (Figure 2c). Elemental mapping confirms the homogeneous distribution of sulfur (S) and tungsten (W) across the monolayer WS_2 sample (Figure 2d). In Figure 2e, super-resolution imaging via state-of-the-art iterative electron ptychography reveals the precise atomic structure of monolayer WS_2, displaying a hexagonal honeycomb pattern with brighter W atoms and less bright atomic columns composed of superimposed twin S atoms. Notably, point W vacancies can be observed, highlighted by the white dashed circle in the image. To explicitly monitor the lattice dynamics under heating, selected area electron diffraction (SAED) patterns were recorded at 15 °C (Figure 2f) and 200 °C (Figure 2g) under identical experimental conditions. The SAED patterns exhibit clear diffraction spots, indicating the characteristic hexagonal lattice symmetry of monolayer WS_2. Subtle changes in lattice spacing with increasing temperature are discernible in reciprocal space, as shown by the evolution of the SAED pattern. These heating-induced lattice dynamics are further illustrated by the difference SAED pattern, especially in an enlarged view of a high-order reflection and its associated intensity profile, provided in Figure 2h. The shift in the high-order reflection of (220) from 7.04 1/nm at 15 °C to 7.14 1/nm at 200 °C in the SAED pattern corresponds to a change of approximately 0.1 1/nm in reciprocal space, revealing an intriguing negative thermal expansion behavior of monolayer WS_2, resulting in a lattice contraction of about 1.4% upon heating (see Note S5).

The observed abnormal negative thermal expansion, in which the lattice contracts rather than expands upon heating, as revealed by straightforward TEM methods, aligns with theoretical studies suggesting that WS_2 exhibits negative thermal expansion coefficients in the range of 200−1000 K due to shifts in specific phonon mode frequencies.[37,38] This thermally induced lattice contraction likely generates internal strain within the WS_2 monolayer. To further explore this, we next conducted density functional theory (DFT) calculations to investigate the changes in electronic structure and effective masses resulting from variations in carrier temperature and lattice strain.

Following photoexcitation of hot carriers, energy is transferred from the carrier subsystem to the lattice, resulting in a decrease in carrier temperature and a corresponding increase in lattice temperature within a few ps[20,39−41] (see Figure 3a and Notes S1 and S2). This process is often accompanied by phenomena such as bandgap renormalization (BGR)[42] and

https://doi.org/10.1021/acsenergylett.5c00307
ACS Energy Lett. 2025, 10, 1741−1750

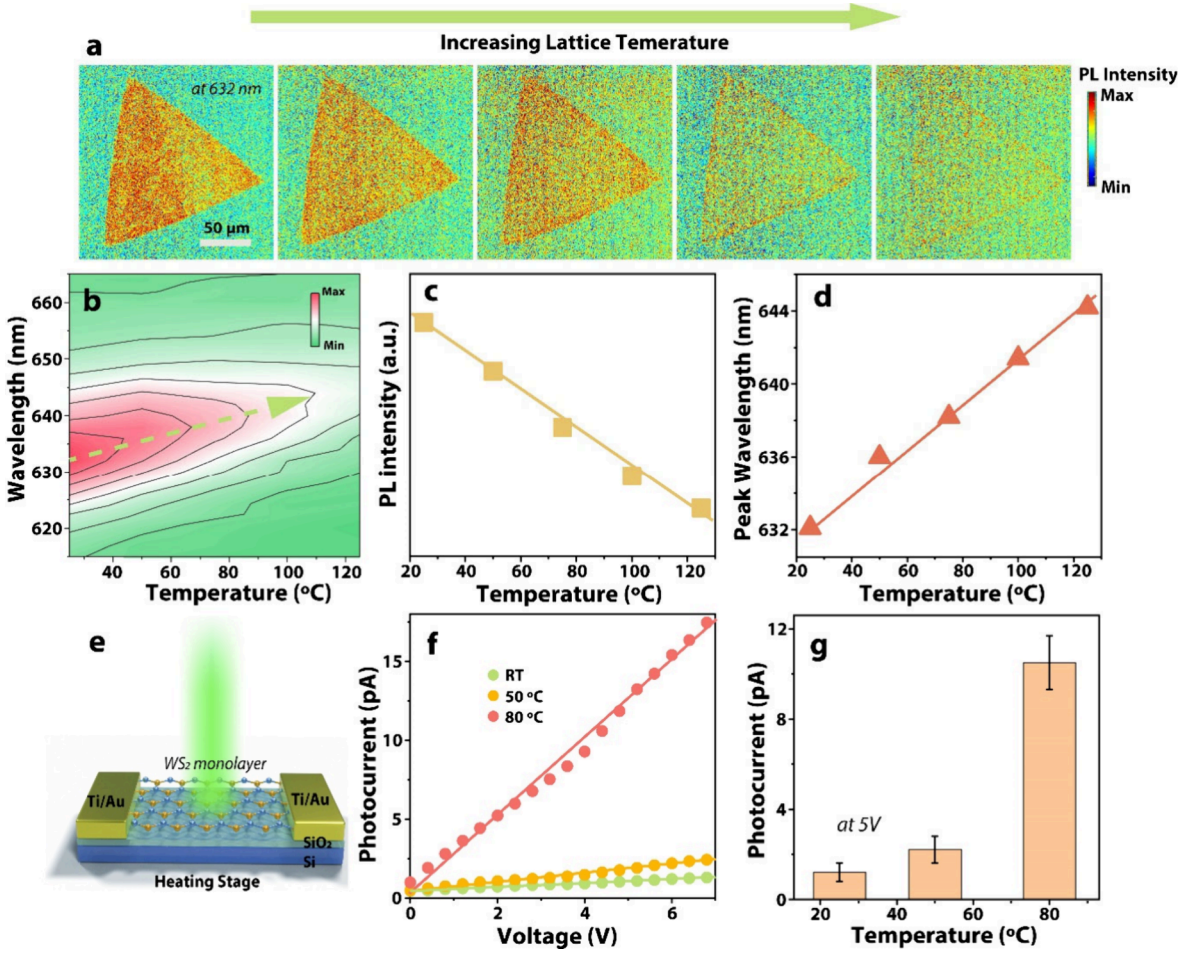

Figure 4. Effect of lattice temperature on PL and photodetector performance. a, Micro-PL imaging with an increasing lattice temperature. The images are selected at the wavelengths of 632 nm, which has the highest intensity at room temperature, and all the images share the same scale bar. b, Lattice temperature-dependent PL spectral map. The dashed arrow indicates the wavelength shift to the lower energy region upon increasing the lattice temperature. c, Lattice temperature-dependent PL intensity changes. d, Lattice temperature-dependent PL peak wavelength shift. e, Schematic illustration of a 2D WS_2 photodetector device fabricated on a SiO_2/Si substrate under 532 nm light illumination. f, Photocurrent response of the typical photodetector at different temperatures, accompanied by linear fits. g, Photocurrent dependence on light intensity at 5 V across three different temperatures. The error bars represent the upper and lower limit values at the selected temperatures.

induces lattice thermal effects that generate internal strain. As positive/negative strain drives these materials toward their atomic limits and simultaneously results in a topologically trivial band structure.[43] To disentangle the photoinduced thermal effects on carrier transport performance, Figure 3b shows the calculated electronic band structures of monolayer WS_2 as a function of electron temperatures, ranging from 1000 to 10000 K. Note that the electron temperature here does not represent the actual physical temperature but rather describes the broadening of electronic occupations around the Fermi level. In contrast, Figure 3c presents the calculated electronic band structures under applied strains varying from 0.5% to 2.0%. Notably, the band structure at an electron temperature of 500 K is nearly identical to that at 1000 K, and the applied strain calculations are based on an electron temperature of 500 K (see Figure S8, calculated at 500 K with 0.0% strain).

In Figure 3b, all depicted monolayer WS_2 structures are direct gap semiconductors, with the band gap (E_g) located at the two inequivalent high-symmetry K points of the hexagonal Brillouin zone (BZ). The corresponding E_g is labeled in each figure, and it is evident that the carrier temperature does not significantly alter the electronic structure of the material. Even at an elevated temperature of 10,000 K, the E_g at the K point only slightly increases, indicating that the band structure is not highly sensitive to photoinduced carrier temperature increases. However, as applied strain increases from 0.0% to 0.5%, there is a substantial reduction in the direct E_g at the K point by ~8.4%, from 1.78 to 1.63 eV, underscoring the strong influence of lattice strain on the electronic properties. Further strains to 1.0%, 1.5%, and 2.0% result in E_g reductions of ~11.8%, 15.2%, and 17.5%, respectively. Additionally, the energy gaps at other symmetry points, such as the M and Γ points, also decrease notably. Based on these observations, we calculated the absorption spectra of monolayer WS_2 under different levels of of applied strains (in Figure 3d, the spectra have been shifted upward for clarity). As expected, the first absorption edge at ~650−700 nm shifts toward the red end of the spectrum, demonstrating enhanced visible light absorption performance and a giant lattice strain-induced BGR. This observation is consistent with previous reports on temperature- and strain-induced BRG effect.[44,45]

https://doi.org/10.1021/acsenergylett.5c00307
ACS Energy Lett. 2025, 10, 1741−1750

The effective masses of electrons and holes in WS_2 at various electron temperatures and strain levels are calculated and presented in Figure 3e,f. From an electron temperature of 500 to 2000 K, there are no observable changes in the effective masses of either electrons or holes. Only when the temperature increases to 5000 K does the effective mass of holes slightly decrease by $0.002m_0$, while that of electrons remains unchanged. This indicates a minimal contribution from photoinduced electron temperature increases to carrier mobilities. However, with the application of strain to the WS_2 lattice due to thermal excitation, from 0.0% to 0.5% (Figure 3f), the effective masses of electrons and holes decrease by ∼2.4% and 1.5%, respectively. This reduction continues as the strain increases to 1.0%, 1.5%, and finally 2.0%, where the effective masses of electrons and holes decrease by ∼5.4% and 3.5%, respectively, indicating enhanced carrier mobilities even with moderate lattice strain. When combined with the fact that photogenerated charge carriers exhibit longer lifetimes at higher lattice temperatures (and thus greater strain), as discussed previously, it can be concluded that the diffusion distance of carriers is significantly extended under photoinduced lattice strain. Moreover, as temperature rises and lattice strain develops, the associated BGR effect is typically accompanied by a reduction in exciton binding energies,[49] driven by the screening of Coulomb interactions by free carriers and increased phonon interactions. The extent of the BGR and the decrease in exciton binding energies are observed to be on the order of tens to hundreds of meV,[46,47] facilitate exciton dissociation and could further enhance carrier transport.

In optoelectronic devices, photoluminescence (PL) performance is a critical metric for assessing device quality and is closely associated with photoinduced carrier transport properties. Charge carrier transport, which can influence the recombination process by localizing carriers, is commonly inversely correlated with PL due to spatial carrier confinement in small domains,[48] particularly in monolayer 2D materials. An increase in photoluminescence (PL) intensity is often linked to a decrease in carrier transport efficiency, as carriers are more likely to undergo radiative recombination instead of diffusing or contributing to nonradiative processes, whereas in photodetectors, carrier transport properties are essential to overall performance,[49] affecting key parameters such as quantum efficiency, responsivity, and others. Therefore, we investigated the impact of lattice temperature on PL and photodetector performance in WS_2 monolayer crystals, as shown in Figure 4.

Figure 4a presents micro-PL images captured at increasing lattice temperatures, all selected at the identical wavelength of 632 nm (Figure S10 displays the images at the peak positions under different temperatures). Figure 4b shows the lattice temperature-dependent PL spectral maps with dashed arrows indicating the wavelength shift. As the lattice temperature rises from room temperature (∼25 °C), the PL intensity continuously decreases dramatically, accompanied by a red shift in the PL peak wavelength (Figure S11). Figure 4 panels c and d depict the PL intensities and wavelength shifts at the maximum position as functions of the lattice temperature, respectively. The PL intensity, which inversely correlates with carrier transport, steadily declines with increasing temperature. Meanwhile, the shift in peak position clearly follows the trend of decreasing energy gaps, consistent with the DFT calculations for lattice strain and corroborating the movement of the negative peak observed in transient spectroscopic measurements (Figure S6e).

The schematic diagram of the fabricated photodetector device is presented in Figure 4e. Ti/Au electrodes were deposited on top of the WS_2 crystal using electron-beam evaporation (see Figure S12), and the devices were mounted on a chip carrier fixture with a heating stage for electrical testing. Figure S13 shows the dark photocurrent curves in the absence of light at three different temperatures, revealing no clear response and independence from temperature. In contrast, Figure 4f illustrates the photoresponse of the device at various lattice temperatures (room temperature, 50 °C, and 80 °C) under identical laser excitation conditions at a wavelength of 532 nm. It is worth noting that the laser was tuned to very low power, and the laser spot was adjusted away from the center of the device to minimize thermal effects caused by laser irradiation. The stability of the on/off cycling, and a single cycle of the photocurrent response which indicates the rise and decay times of the device, are shown in Figure S14. In Figure 4f, the device exhibits an extremely low current of ∼1.2 pA at 5 V under room temperature conditions, which increases markedly as the temperature rises (Figure 4g). Given the relatively low response due to weak illumination intensity and the inherent noise level of the instrumentation, we estimate that the photocurrent intensity is enhanced by ∼10 times when the temperature is elevated from room temperature to 80 °C. This enhancement is likely driven by lattice temperature-induced improvements in carrier transport, analogous to how photoinduced thermal effects facilitate ultrafast surface carrier diffusion. Although other intertwined temperature-induced factors, such as changes in the electronic, optical, and structural properties of the device, may also affect the outcome. Nevertheless, the general picture of increasing lattice temperature leading to improved photodetector performance is consistent with DFT calculations, temperature-dependent PL experiments, and previously discussed SUEM results.

In summary, we have uncovered a critical mechanism by which photoinduced negative thermal expansion in monolayer WS_2 enhances surface carrier transport, utilizing a novel surface-sensitive SUEM technique and *in situ* super-resolution STEM ptychography with atomic-spatial resolution. Unlike conventional photon-pump/photon-probe charge carrier mapping methods, which are limited by large penetration depths and their inability to probe the subtle yet crucial surface dynamics, SUEM captures ultrafast dynamics at the atomic surface, making it particularly relevant for 2D materials. Our results reveal that, in monolayer 2D WS_2, charge carrier diffusion is primarily confined to the first tens of picoseconds following photoexcitation, during which the system remains thermally active due to carrier−lattice interactions. Importantly, we have discovered that photoinduced negative thermal expansion, driven by local heating, generates internal strain, substantially modifies the electronic structure, and reduces the effective masses of both electrons and holes, thereby markedly improving carrier transport efficiency and an order-of-magnitude improvement in photodetection performance. While the rise in temperature may concurrently lead to increased carrier scattering and other commensurate secondary effects, our findings show that the direct impact of carrier temperature is minimal. This distinctive phenomenon of lattice negative expansion bears similarities to the electrostrictive response observed in methylammonium lead triiodide

https://doi.org/10.1021/acsenergylett.5c00307
ACS Energy Lett. 2025, 10, 1741−1750

($MAPbI_3$) single crystals,[50] where compressive strain arises from lattice deformation under applied bias. However, this study represents the first direct observation of the behavior in 2D materials. Our findings outline a clear and effective approach for optimizing photoexcitation conditions to improve the performance of WS_2-based optoelectronic devices. Furthermore, the insights gained from this research are likely to be applicable across various TMD materials, providing new strategies for advancing next-generation optoelectronics.

■ ASSOCIATED CONTENT

Supporting Information

The Supporting Information is available free of charge at https://pubs.acs.org/doi/10.1021/acsenergylett.5c00307.

Experimental methods, DFT calculations, fitting procedures, supplementary notes (photo-induced thermal effects, estimation of photo-induced lattice temperature increase, fitting of dynamics in SUEM and TR experiments, decay-associated spectra and lifetime density analysis, determination of lattice negative thermal expansion via TEM measurements); SUEM difference images and signals, spatial distance maps, FWHM evolution, time-resolved optical spectroscopy, transient reflectivity spectra, band structures, band gap dependence on strain, micro-PL imaging, PL spectra, optical microscope images, photocurrent data; table of TR temporal trace parameters (PDF)

■ AUTHOR INFORMATION

Corresponding Authors

Yihan Zhu − *Center for Electron Microscopy, State Key Laboratory Breeding Base of Green Chemistry Synthesis Technology and College of Chemical Engineering, Zhejiang University of Technology, Hangzhou 310014 Zhejiang, China*; Email: yihanzhu@zjut.edu.cn

Omar F. Mohammed − *Center for Renewable Energy and Storage Technologies, Division of Physical Science and Engineering, King Abdullah University of Science and Technology (KAUST), Thuwal 23955-6900, Saudi Arabia*; orcid.org/0000-0001-8500-1130; Email: omar.abdelsaboor@kaust.edu.sa

Authors

Lijie Wang − *Center for Renewable Energy and Storage Technologies, Division of Physical Science and Engineering, King Abdullah University of Science and Technology (KAUST), Thuwal 23955-6900, Saudi Arabia*; orcid.org/0000-0002-1786-5962

Yue Liu − *Center for Electron Microscopy, State Key Laboratory Breeding Base of Green Chemistry Synthesis Technology and College of Chemical Engineering, Zhejiang University of Technology, Hangzhou 310014 Zhejiang, China*

Jie Yang − *Key Laboratory of Material Physics, Ministry of Education, School of Physics, Zhengzhou University, Zhengzhou 450001, China*

Xiangming Xu − *Center for Renewable Energy and Storage Technologies, Division of Physical Science and Engineering, King Abdullah University of Science and Technology (KAUST), Thuwal 23955-6900, Saudi Arabia*; orcid.org/0000-0002-8047-8244

Bingyao Shao − *Center for Renewable Energy and Storage Technologies, Division of Physical Science and Engineering, King Abdullah University of Science and Technology (KAUST), Thuwal 23955-6900, Saudi Arabia*; orcid.org/0000-0002-9334-3592

Hongwei Zhu − *Center for Renewable Energy and Storage Technologies, Division of Physical Science and Engineering, King Abdullah University of Science and Technology (KAUST), Thuwal 23955-6900, Saudi Arabia*; orcid.org/0000-0002-2741-5172

Haiting Cai − *Center for Electron Microscopy, State Key Laboratory Breeding Base of Green Chemistry Synthesis Technology and College of Chemical Engineering, Zhejiang University of Technology, Hangzhou 310014 Zhejiang, China*

Tulai Sun − *Center for Electron Microscopy, State Key Laboratory Breeding Base of Green Chemistry Synthesis Technology and College of Chemical Engineering, Zhejiang University of Technology, Hangzhou 310014 Zhejiang, China*

Jun Yin − *Department of Applied Physics, The Hong Kong Polytechnic University, Kowloon 999077 Hong Kong SAR, China*; orcid.org/0000-0002-1749-1120

Husam N. Alshareef − *Center for Renewable Energy and Storage Technologies, Division of Physical Science and Engineering, King Abdullah University of Science and Technology (KAUST), Thuwal 23955-6900, Saudi Arabia*; orcid.org/0000-0001-5029-2142

Osman M. Bakr − *Center for Renewable Energy and Storage Technologies, Division of Physical Science and Engineering, King Abdullah University of Science and Technology (KAUST), Thuwal 23955-6900, Saudi Arabia*; orcid.org/0000-0002-3428-1002

Complete contact information is available at: https://pubs.acs.org/10.1021/acsenergylett.5c00307

Notes

The authors declare no competing financial interest.

■ ACKNOWLEDGMENTS

This work was supported by King Abdullah University of Science and Technology (KAUST). Y. Liu, H. Cai, T. Sun and Y. Zhu acknowledge National Key Research and Development Program of China (2022YFE0113800) and the National Natural Science Foundation of China (22122505, 22075250, 21771161). J. Yang acknowledges financial support from the National Natural Science Foundation of China (No. 12347160), the Key Scientific Research Project of Colleges and Universities in He'nan Province (No. 24A140022), and the Natural Science Foundation of He'nan (No. 242300421671). J. Yin acknowledges financial support from Hong Kong Polytechnic University (grant no. P0042930, P0050410 and P0053682) and grants from the Research Grants Council of the Hong Kong Special Administrative Region, China (project no. PolyU 25300823 and PolyU 15300724), and National Natural Science Foundation of China (62422512).

■ REFERENCES

(1) Gao, Y.; Liang, H.; Xu, H.; Cui, D.; Wu, C.; Chen, J.; Liu, Y.; Dou, S.; Huang, W.; Lin, L. Emerging Amorphized Metastable Structures to Break Limitations of 2D Materials for More Promising Electrocatalysis. *ACS Energy Lett.* **2024**, *9* (8), 3982−4002.

(2) Wang, Y.; Chhowalla, M. Making Clean Electrical Contacts on 2D Transition Metal Dichalcogenides. *Nat. Rev. Phys.* **2022**, *4* (2), 101−112.
(3) Wang, Y.; Sarkar, S.; Yan, H.; Chhowalla, M. Critical Challenges in the Development of Electronics Based on Two-Dimensional Transition Metal Dichalcogenides. *Nat. Electron* **2024**, *7* (8), 638−645.
(4) Hong, C.; Oh, S.; Dat, V. K.; Pak, S.; Cha, S.; Ko, K.-H.; Choi, G.-M.; Low, T.; Oh, S.-H.; Kim, J.-H. Engineering Electrode Interfaces for Telecom-Band Photodetection in MoS_2/Au Heterostructures via Sub-Band Light Absorption. *Light Sci. Appl.* **2023**, *12* (1), 280.
(5) Pendurthi, R.; Sakib, N. U.; Sadaf, M. U. K.; Zhang, Z.; Sun, Y.; Chen, C.; Jayachandran, D.; Oberoi, A.; Ghosh, S.; Kumari, S.; Stepanoff, S. P.; Somvanshi, D.; Yang, Y.; Redwing, J. M.; Wolfe, D. E.; Das, S. Monolithic Three-Dimensional Integration of Complementary Two-Dimensional Field-Effect Transistors. *Nat. Nanotechnol.* **2024**, *19* (7), 970−977.
(6) Chowdhury, T.; Sadler, E. C.; Kempa, T. J. Progress and Prospects in Transition-Metal Dichalcogenide Research Beyond 2D. *Chem. Rev.* **2020**, *120* (22), 12563−12591.
(7) Zhu, Y.; Prezhdo, O. V.; Long, R.; Fang, W.-H. Twist Angle-Dependent Intervalley Charge Carrier Transfer and Recombination in Bilayer WS_2. *J. Am. Chem. Soc.* **2023**, *145* (41), 22826−22835.
(8) Dutta, R.; Bala, A.; Sen, A.; Spinazze, M. R.; Park, H.; Choi, W.; Yoon, Y.; Kim, S. Optical Enhancement of Indirect Bandgap 2D Transition Metal Dichalcogenides for Multi-Functional Optoelectronic Sensors. *Adv. Mater.* **2023**, *35* (46), No. 2303272.
(9) Herman, A. P.; Zelewski, S. J.; Misztal, K.; Kudrawiec, R. Probing the Long-Lived Photo-Generated Charge Carriers in Transition Metal Dichalcogenides by Time-Resolved Microwave Photoconductivity. *Nanophotonics* **2022**, *11* (7), 1335−1344.
(10) Zhang, L.; Liu, J.; Jiang, H.; Gu, H.; Liu, S. Layer-Dependent Photoexcited Carrier Dynamics of WS_2 Observed Using Single Pulse Pump Probe Method. *Chin. Opt. Lett., COL* **2022**, *20* (10), No. 100002.
(11) Wen, X.; Chen, S.; Zhao, J.; Du, W.; Zhao, W. Enhanced Plasmonic Hot-Carrier Transfer in Au/WS_2 Heterojunctions under Nonequilibrium Condition. *ACS Photonics* **2022**, *9* (5), 1522−1528.
(12) Wang, T.; Hopper, T. R.; Mondal, N.; Liu, S.; Yao, C.; Zheng, X.; Torrisi, F.; Bakulin, A. A. Hot Carrier Cooling and Trapping in Atomically Thin WS_2 Probed by Three-Pulse Femtosecond Spectroscopy. *ACS Nano* **2023**, *17* (7), 6330−6340.
(13) Liang, Y.; Zhang, G.; Sun, J.; Zhou, C.; Li, Z.; Ye, Y.; Yang, X.; Ren, Z. Carrier Dynamics in the Space Charge Layer of MoS_2 Flakes Studied by Time-Resolved μ-Surface Photovoltage. *J. Phys. Chem. C* **2023**, *127* (15), 7319−7326.
(14) Niemeyer, M.; Ohlmann, J.; Walker, A. W.; Kleinschmidt, P.; Lang, R.; Hannappel, T.; Dimroth, F.; Lackner, D. Minority Carrier Diffusion Length, Lifetime and Mobility in p-Type GaAs and GaInAs. *J. Appl. Phys.* **2017**, *122* (11), No. 115702.
(15) Yang, D.; Ming, W.; Shi, H.; Zhang, L.; Du, M.-H. Fast Diffusion of Native Defects and Impurities in Perovskite Solar Cell Material $CH_3NH_3PbI_3$. *Chem. Mater.* **2016**, *28* (12), 4349−4357.
(16) Shrestha, S.; Li, X.; Tsai, H.; Hou, C.-H.; Huang, H.-H.; Ghosh, D.; Shyue, J.-J.; Wang, L.; Tretiak, S.; Ma, X. Long Carrier Diffusion Length in Two-Dimensional Lead Halide Perovskite Single Crystals. *Chem.* **2022**, *8* (4), 1107−1120.
(17) Li, M.; Chen, J.-S.; Cotlet, M. Light-Induced Interfacial Phenomena in Atomically Thin 2D van Der Waals Material Hybrids and Heterojunctions. *ACS Energy Lett.* **2019**, *4* (9), 2323−2335.
(18) Chen, K.; Roy, A.; Rai, A.; Movva, H. C.; Meng, X.; He, F.; Banerjee, S. K.; Wang, Y. Accelerated Carrier Recombination by Grain Boundary/Edge Defects in MBE Grown Transition Metal Dichalcogenides. *APL Materials* **2018**, *6* (5), No. 056103.
(19) Yuan, L.; Huang, L. Exciton Dynamics and Annihilation in WS_2 2D Semiconductors. *Nanoscale* **2015**, *7* (16), 7402−7408.
(20) Liu, Q.; Wei, K.; Tang, Y.; Xu, Z.; Cheng, X.; Jiang, T. Visualizing Hot-Carrier Expansion and Cascaded Transport in WS_2 by Ultrafast Transient Absorption Microscopy. *Advanced Science* **2022**, *9* (10), No. 2105746.
(21) Wei, X.; Wang, Z.; Wang, Z.; Lu, Y.; Ji, Q.; Liu, W. Unveiling Spatiotemporal Diffusion of Hot Carriers Influenced by Spatial Nonuniform Hot Phonon Bottleneck Effect in Monolayer MoS_2. *Nano Lett.* **2024**, *24* (30), 9269−9275.
(22) Snaider, J. M.; Guo, Z.; Wang, T.; Yang, M.; Yuan, L.; Zhu, K.; Huang, L. Ultrafast Imaging of Carrier Transport across Grain Boundaries in Hybrid Perovskite Thin Films. *ACS Energy Lett.* **2018**, *3* (6), 1402−1408.
(23) Kumar, N.; Cui, Q.; Ceballos, F.; He, D.; Wang, Y.; Zhao, H. Exciton Diffusion in Monolayer and Bulk $MoSe_2$. *Nanoscale* **2014**, *6* (9), 4915−4919.
(24) Perez, C.; Ellis, S. R.; Alcorn, F. M.; Smoll, E. J.; Fuller, E. J.; Leonard, F.; Chandler, D.; Talin, A. A.; Bisht, R. S.; Ramanathan, S.; Goodson, K. E.; Kumar, S. Picosecond Carrier Dynamics in InAs and GaAs Revealed by Ultrafast Electron Microscopy. *Science Advances* **2024**, *10* (20), No. eadn8980.
(25) Wang, L.; Nughays, R.; Song, X.; Bian, T.; Hedhili, M. N.; Yin, J.; Bakr, O. M.; Mohammed, O. F. Crystallographic Orientation-Dependent Photo-Response of Planar Cadmium Telluride X-Ray Detectors. *Cell Reports Physical Science* **2023**, *4* (12), No. 101723.
(26) Garming, M. W.; Weppelman, I. G. C.; Lee, M.; Stavenga, T.; Hoogenboom, J. P. Ultrafast Scanning Electron Microscopy with Sub-Micrometer Optical Pump Resolution. *Applied Physics Reviews* **2022**, *9* (2), No. 021418.
(27) Bose, R.; Adhikari, A.; Burlakov, V. M.; Liu, G.; Haque, M. A.; Priante, D.; Hedhili, M. N.; Wehbe, N.; Zhao, C.; Yang, H. Imaging Localized Energy States in Silicon-Doped InGaN Nanowires Using 4D Electron Microscopy. *ACS Energy Letters* **2018**, *3* (2), 476−481.
(28) Liao, B.; Najafi, E.; Li, H.; Minnich, A. J.; Zewail, A. H. Photo-Excited Hot Carrier Dynamics in Hydrogenated Amorphous Silicon Imaged by 4D Electron Microscopy. *Nat. Nanotechnol.* **2017**, *12* (9), 871−876.
(29) Liao, B.; Zhao, H.; Najafi, E.; Yan, X.; Tian, H.; Tice, J.; Minnich, A. J.; Wang, H.; Zewail, A. H. Spatial-Temporal Imaging of Anisotropic Photocarrier Dynamics in Black Phosphorus. *Nano Lett.* **2017**, *17* (6), 3675−3680.
(30) Yang, D.-S.; Liao, B.; Mohammed, O. F. Scanning Ultrafast Electron Microscopy: Four-Dimensional Imaging of Materials Dynamics in Space and Time. *MRS Bull.* **2018**, *43* (7), 491−496.
(31) Sun, J.; Melnikov, V. A.; Khan, J. I.; Mohammed, O. F. Real-Space Imaging of Carrier Dynamics of Materials Surfaces by Second-Generation Four-Dimensional Scanning Ultrafast Electron Microscopy. *J. Phys. Chem. Lett.* **2015**, *6* (19), 3884−3890.
(32) Wang, L.; Nughays, R.; Rossi, T. C.; Oppermann, M.; Ogieglo, W.; Bian, T.; Shih, C.-H.; Guo, T.-F.; Pinnau, I.; Yin, J.; Bakr, O. M.; Mohammed, O. F.; Chergui, M. Disentangling Thermal from Electronic Contributions in the Spectral Response of Photoexcited Perovskite Materials. *J. Am. Chem. Soc.* **2024**, *146* (8), 5393−5401.
(33) Liu, J.; Leng, J.; Wang, S.; Zhang, J.; Jin, S. Artifacts in Transient Absorption Measurements of Perovskite Films Induced by Transient Reflection from Morphological Microstructures. *J. Phys. Chem. Lett.* **2019**, *10* (1), 97−101.
(34) Price, M. B.; Butkus, J.; Jellicoe, T. C.; Sadhanala, A.; Briane, A.; Halpert, J. E.; Broch, K.; Hodgkiss, J. M.; Friend, R. H.; Deschler, F. Hot-Carrier Cooling and Photoinduced Refractive Index Changes in Organic−Inorganic Lead Halide Perovskites. *Nat. Commun.* **2015**, *6* (1), 8420.
(35) Chen, X.; Kamat, P. V.; Janáky, C.; Samu, G. F. Charge Transfer Kinetics in Halide Perovskites: On the Constraints of Time-Resolved Spectroscopy Measurements. *ACS Energy Lett.* **2024**, *9* (6), 3187−3203.
(36) Li, Y.; Shi, J.; Chen, H.; Wang, R.; Mi, Y.; Zhang, C.; Du, W.; Zhang, S.; Liu, Z.; Zhang, Q. The Auger Process in Multilayer WSe_2 Crystals. *Nanoscale* **2018**, *10* (37), 17585−17592.
(37) Ding, Y.; Xiao, B. Thermal Expansion Tensors, Grüneisen Parameters and Phonon Velocities of Bulk MT_2 (M= W and Mo; T=

https://doi.org/10.1021/acsenergylett.5c00307
ACS Energy Lett. 2025, 10, 1741−1750

S and Se) from First Principles Calculations. *RSC Adv.* **2015**, *5* (24), 18391−18400.
(38) Kumar, D.; Singh, B.; Kumar, P.; Balakrishnan, V.; Kumar, P. Thermal Expansion Coefficient and Phonon Dynamics in Coexisting Allotropes of Monolayer WS_2 Probed by Raman Scattering. *J. Phys.: Condens. Matter* **2019**, *31* (50), No. 505403.
(39) Sadasivam, S.; Chan, M. K. Y.; Darancet, P. Theory of Thermal Relaxation of Electrons in Semiconductors. *Phys. Rev. Lett.* **2017**, *119* (13), No. 136602.
(40) Ruppert, C.; Chernikov, A.; Hill, H. M.; Rigosi, A. F.; Heinz, T. F. The Role of Electronic and Phononic Excitation in the Optical Response of Monolayer WS_2 after Ultrafast Excitation. *Nano Lett.* **2017**, *17* (2), 644−651.
(41) Jöbsis, H. J.; Gao, L.; Reponen, A.-P. M.; VanOrman, Z. A.; Rijpers, R. P. P. P. M.; Wang, H. I.; Feldmann, S.; Hutter, E. M. The Effect of Charge Carrier Cooling on the Ultrafast Carrier Dynamics in $Cs_2AgBiBr_6$ Thin Films. *ACS Energy Lett.* **2025**, *10* (2), 1050−1056.
(42) Chernikov, A.; Ruppert, C.; Hill, H. M.; Rigosi, A. F.; Heinz, T. F. Population Inversion and Giant Bandgap Renormalization in Atomically Thin WS_2 Layers. *Nat. Photonics* **2015**, *9* (7), 466−470.
(43) Chen, S.; Parker, I. J.; Monserrat, B. Temperature Effects in Topological Insulators of Transition Metal Dichalcogenide Monolayers. *Phys. Rev. B* **2024**, *109* (15), No. 155125.
(44) Sun, Z.; Beaumariage, J.; Movva, H. C.; Chowdhury, S.; Roy, A.; Banerjee, S. K.; Snoke, D. W. Stress-Induced Bandgap Renormalization in Atomic Crystals. *Solid State Commun.* **2019**, *288*, 18−21.
(45) Mishra, H.; Bose, A.; Dhar, A.; Bhattacharya, S. Exciton-Phonon Coupling and Band-Gap Renormalization in Monolayer WSe_2. *Phys. Rev. B* **2018**, *98* (4), No. 045143.
(46) Chernikov, A.; van der Zande, A. M.; Hill, H. M.; Rigosi, A. F.; Velauthapillai, A.; Hone, J.; Heinz, T. F. Electrical Tuning of Exciton Binding Energies in Monolayer WS_2. *Phys. Rev. Lett.* **2015**, *115* (12), No. 126802.
(47) Zhang, C.; Johnson, A.; Hsu, C.-L.; Li, L.-J.; Shih, C.-K. Direct Imaging of Band Profile in Single Layer MoS_2 on Graphite: Quasiparticle Energy Gap, Metallic Edge States, and Edge Band Bending. *Nano Lett.* **2014**, *14* (5), 2443−2447.
(48) Stoddard, R. J.; Eickemeyer, F. T.; Katahara, J. K.; Hillhouse, H. W. Correlation between Photoluminescence and Carrier Transport and a Simple In Situ Passivation Method for High-Bandgap Hybrid Perovskites. *J. Phys. Chem. Lett.* **2017**, *8* (14), 3289−3298.
(49) Gao, J.; Rao, A. M.; Li, H.; Zhang, J.; Chen, O. Carrier Transport Dynamics in High Speed Black Phosphorus Photodetectors. *ACS Photonics* **2018**, *5* (4), 1412−1417.
(50) Chen, B.; Li, T.; Dong, Q.; Mosconi, E.; Song, J.; Chen, Z.; Deng, Y.; Liu, Y.; Ducharme, S.; Gruverman, A. Large Electrostrictive Response in Lead Halide Perovskites. *Nature materials* **2018**, *17* (11), 1020−1026.

https://doi.org/10.1021/acsenergylett.5c00307
ACS Energy Lett. 2025, 10, 1741−1750